Ripening and Focusing of Aggregate Size Distributions with Overall Volume Growth

J. Vollmer,[1,2] A. Papke,[1,2] and M. Rohloff[1,2]
[1]*Max Planck Institute for Dynamics and Self-Organization (MPI DS), Göttingen, Germany*
[2]*Faculty of Physics, Georg-August Univ. Göttingen, Göttingen, Germany*

(Dated: March 12, 2014 — 1:03am)

We explore the evolution of the aggregate size distribution in systems where aggregates grow by diffusive accretion of mass. Supersaturation is controlled in such a way that the overall aggregate volume grows linearly in time. Classical Ostwald ripening, which is recovered in the limit of vanishing overall growth, constitutes an unstable solution of the dynamics. In the presence of overall growth evaporation of aggregates always drives the dynamics into a new, qualitatively different growth regime where ripening ceases, and growth proceeds at a constant number density of aggregates. We provide a comprehensive description of the evolution of the aggregate size distribution in the constant density regime: the size distribution does not approach a universal shape, and even for moderate overall growth rates the standard deviation of the aggregate radius decays monotonically. The implications of this theory for the focusing of aggregate size distributions are discussed for a range of different settings including the growth of tiny rain droplets in clouds, as long as they do not yet feel gravity, and the synthesis of nano-particles and quantum dots.

arXiv:1403.2661v1 [cond-mat.stat-mech] 11 Mar 2014

I. INTRODUCTION

Characterising the evolution of the number density and the size distribution of an assembly of aggregates in a fluid or solid matrix has intrigued chemists (Johnson *et al.*, 2012; Kahlweit, 1976; Wagner, 1961), physicists (Bray, 1994; Lifshitz and Slyozov, 1961; Shneidman, 2013; Slezov, 2009), and applied mathematicians (Goudon *et al.*, 2012; Niethammer and Pego, 1999; Penrose, 1997; Smereka, 2008; Voorhees, 1985) since it was first described by Ostwald (1900). Early successes in the theoretical modeling focused on describing the diffusive transport of material to the aggregates (LaMer and Dinegar, 1950). In many applications the volume fraction of the aggregates grows in time — either due to feeding by a chemical reaction, or because temperature or pressure changes lead to a change of the equilibrium volume fraction of the aggregates. Reiss (1951) pointed out that the resulting sustained growth of the volume fraction of the aggregates can lead to focusing of the aggregate size distribution (see Clark *et al.*, 2011; Kwon and Hyeon, 2011; Sowers *et al.*, 2013, for recent discussions). Subsequent theoretical work focused on the ripening of the aggregate size distribution under thermodynamic equilibrium conditions, where to a good approximation the aggregate volume fraction is preserved (Lifshitz and Slyozov, 1961; Wagner, 1961). This dynamics involves aggregate ripening, a delicate balance of the evaporation of small aggregates, and the redistribution of their volume to achieve further growth of large aggregates. Assembly expectation values do not only change due to the evolution of the shape of the size distribution, but also by the change of its normalisation, i.e., the number of aggregates. Independently, Lifshitz and Slyozov (1961) and Wagner (1961) derived scaling laws for the decay of the number of aggregates, and the resulting growth speed of the mean aggregate radius, and they determined the shape of the asymptotic size distribution. Modern expositions derive their results from the point of view of dynamic scaling theory (Barenblatt, 2003; Bray, 1994; Voorhees, 1985).

Here, we revisit the problem of simultaneous growth and coarsening in the presence of overall volume growth. The increase of the aggregate volume fraction can be provided by different mechanisms: **(i)** a change of ambient temperature or pressure that drives the system deeper into a miscibility gap (Cates *et al.*, 2003; Vollmer *et al.*, 2007, 1997), **(ii)** evaporation of small particles denoted as *sacrificial nano-particles*, that are continuously added to the system (Johnson *et al.*, 2012), or **(iii)** a chemical reaction or external flux of material into the system (*cf.* the review of Sowers *et al.*, 2013). Depending on context the aggregates may be bubbles, droplets or solid aggregates. However, in any case we consider aggregate growth for dilute systems where merging of aggregates and sedimentation play a negligible role.

We idealise aggregate growth and ripening by considering the setting of a sustained constant flux onto the aggregates (Nozawa *et al.*, 2005) which gives rise to a linear growth of the aggregate volume fraction. For the phase separation of binary mixtures such a setting has been studied experimentally by Auernhammer *et al.* (2005) and Lapp *et al.* (2012). The present work establishes that the net volume growth leads to a cross over to behaviour that is remarkably different from the behaviour assumed in dynamic scaling theory.

We present a new numerical algorithm that allows us to follow the aggregate growth up to five orders of magnitude in the volume – *i.e.* we cover a factor of 50 in their average radius, $\langle R\rangle$. This large range is needed to settle in the asymptotic scaling regime where the form of the aggregate size distribution, and the exponents of the power-law growth describing the aggregate number density and the average volume can credibly be tested. To gain insight into the impact of the net aggregate growth, we explore the evolution of the size distribution for growth speeds, ξ, of the aggregate volume fraction that cover a range of three orders of magnitude.

Based on our numerical study we set up a theoretical analysis that is based on the evolution of the reduced aggregate radius, $\rho = R/\langle R\rangle$. In line with Clark *et al.* (2011)'s findings the ratio

$$k = \frac{\langle R\rangle}{R_c} = 1 + \frac{\xi}{4\pi\ \sigma D\ n} \tag{1}$$

of the average aggregate radius $\langle R\rangle$ and the critical radius R_c,

that separates the size of aggregates that grow from those that shrink, is identified as the relevant control parameter that governs the evolution. For equilibrium systems the overall aggregate volume is preserved such that $\xi = 0$ and $k = 1$. When there is a net growth of the overall aggregate volume, the control parameter k is increased by the ratio of the growth rate ξ and the diffusive relaxation rate of supersaturation, $4\pi\,\sigma D\,n$ where n is the number density of aggregates, D is the diffusion coefficient relevant for the transport of material to the aggregates, and σ is a length scale of the order of the interface width (*cf.* Bray, 1994; Landau and Lifshitz, 1983, and Sec. II.A for details). In Fig. 1 we provide a central result of the present study, the phase portrait of the flow of ρ at a constant k, which will be derived and discussed in full detail in Sec. IV. Ripening at a fixed aggregate volume fraction, *i.e.* for $\xi = 0$, amounts to the control parameter $k = 1$. In this case $R_c = \langle R\rangle$ as pointed out by Lifshitz and Slyozov (1961). For $\xi \simeq 0$, ripening arises by the interplay of an unstable fixed point of the evolution for $\rho = 1$ which enforces evaporation of small aggregates, and the constraint of the overall conservation of volume that limits the growth of the larger aggregates (Slezov, 2009, Chap. 7). Beyond $k = 3/2$ this behaviour changes qualitatively due to an exchange of stability bifurcation where the fixed point $\rho = 1$ becomes stable. In the following the consequences of this exchange on the asymptotic form and evolution of the aggregate size distribution are explicitly worked out, and compared to the numerical data.

The phase diagram, Fig. 1, demonstrates how our discussion provides a fresh view on a number of applications that are under very active research presently: A common feature of recipes for the synthesis of nano-particles with narrow size distributions is that the focusing results from aggregate growth proceeding in the presence of sustained mass flux, that is reflected in an overall growth of the aggregate volume (Clark *et al.*, 2011; Jana *et al.*, 2013; Johnson *et al.*, 2012; Nozawa *et al.*, 2005). In the chemical application one exploits transient focusing of the polydispersity of the larger particles in bidisperse distributions (Johnson *et al.*, 2012; Ludwig and Schmelzer, 1995), and in systems where there is a considerable net flux onto the aggregates (Jana *et al.*, 2013; Peng *et al.*, 1998; Reiss, 1951; Sugimoto, 1987). In these recipes the coarsening must be stopped once the chemical precursor reaction that provides the material condensing on the aggregates starts to cease. We argue that this is done when k drops below $3/2$. Ripening would otherwise lead to a broadening of the very sharp aggregate size distributions such that eventually they approach the asymptotic Lifshitz and Slyozov (1961) distribution (see the review Sowers *et al.*, 2013).

Systems with a sustained flux onto the aggregates are also commonly encountered in the ripening and growth of bubbles in soda drinks, beer and sparkling wine (Soltzberg *et al.*, 1997; Zhang and Xu, 2008), and in many natural processes. Noticeable examples in the geo-sciences are the ripening and growth of bubbles in the depths of geysers prior to eruption (Han *et al.*, 2013; Ingebritsen and Rojstaczer, 1993; Toramaru and Maeda, 2013), and the growth of bubbles (Manga, 1996) and crystallites in cooling magma (Martin and Nokes, 1988; Sparks and Huppert, 1987).

The paper is organised as follows: In Sec. II we derive the equations of motion for the aggregate radius, and explain how

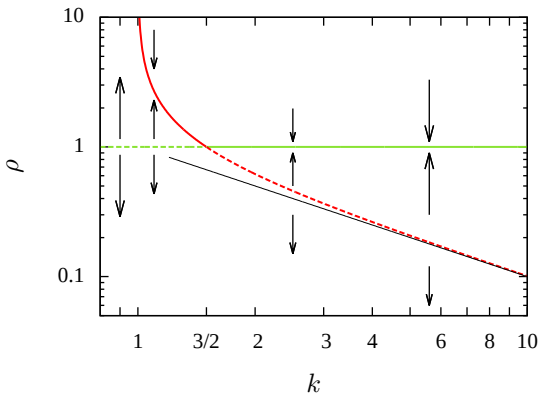

Figure 1 Phase portrait of the evolution of the reduced aggregate radius $\rho = R/\langle R\rangle$. Dashed lines denote unstable fixed points, and solid line stable ones. The green lines denotes a fixed point at $\rho = 1$, and the red lines the position of another fixed point, ρ_+, defined in Eq. (16b). A thin straight black line has been added to show that ρ_+ rapidly approaches k^{-1} for $k \gtrsim 5$.

the equations are integrated numerically. For N aggregates the evolution is provided by a set of N non-linear differential equations for the respective radii. The equations are coupled because they involve moments of the size distribution. A theoretical description of the time evolution of the aggregate size distribution is obtained in three steps: In Sec. III we explore the time evolution of the relevant moments of the aggregate size distribution. This allows us in Sec. IV to solve the evolution of the size of individual aggregates *constrained* to the time evolution of the moments. Hence, we reduce the problem of solving the set of N equations to finding the solutions of a single non-linear differential equation for N different initial conditions, which define the initial aggregate size distribution. At this point we also explore the consequences the exchange of stability bifurcation on the evaporation of aggregates. Subsequently, in Sec. V we combine the results on the evolution of the moments and on the resulting evolution of the size of individual aggregates to obtain the evolution of the aggregate size distribution. In each step of this analysis we compare the predictions to the numerical data. The implications of our findings on different experimental systems are discussed in Sec. VI, and the the prime results of our study are summarised in Sec. VII.

II. THE ASSEMBLY OF AGGREGATE RADII

In principle many different processes contribute to aggregate growth. Here, we consider the case where

- there are sufficiently few aggregates such that they grow by diffusive flux received from a mean-field background supersaturation field — analogously to Lifshitz-Slyozov-Wagner theory (Bray, 1994)
- the feeding rate, ξ, is sufficiently small such that it only affects the mean-field level of supersaturation, and does not interfere with the diffusion coupling the aggregates to the supersaturation (*cf.* Vollmer, 2008, for a discussion of potential changes to the diffusion equation).

A. Evolution of the aggregate radii and their volume

The supersaturation in the bulk is relaxed by diffusion onto the aggregates, causing them to grow. Following Bray (1994); Landau and Lifshitz (1983), we have

$$\dot{R} = \frac{\sigma D}{R^2}\ \left[\frac{R}{R_c} - 1\right] . \tag{2}$$

Here, R_c is the critical aggregate radius which depends on the supersaturation in the system, D is the pertinent concentration diffusion coefficient, and σ is a microscopic length scale which accounts for the aggregate-size dependence of the chemical potential drop that is driving the diffusive fluxes. Specifically, σ is proportional to the interfacial tension. Its full parameter dependence and characteristic values for some typical applications are provided in Sec. VI.

The term in square brackets in Eq. (2) accounts for the effect of interfacial tension on aggregate growth. Interfacial tension penalises small aggregates such that only aggregates with a radius larger than R_c can grow. For instance, in Lifshitz-Slyozov-Wagner theory no supersaturation is provided externally, and R_c is equal to the average radius $\langle R\rangle$. Smaller aggregates evaporate, and hence they provides the supersaturation which admits the growth of the larger aggregates.

Let us now consider the evolution of N aggregates of respective radius R_i, $i = 1 \dots N$. Their total volume is

$$V = \frac{4\pi}{3} \sum_{i=1}^{N} R_i^3 . \tag{3a}$$

Introducing the average aggregate radius, $\langle R\rangle = N^{-1} \sum_i R_i$, one finds

$$\begin{aligned} \dot{V} &= 4\pi \sum_i R_i^2 \dot{R}_i = 4\pi\ \sigma D\ \sum_i \left[\frac{R_i}{R_c} - 1\right] \\ &= 4\pi\ \sigma D\ N\ \left[\frac{\langle R\rangle}{R_c} - 1\right] = 4\pi\ \sigma D\ N\ (k-1) , \end{aligned} \tag{3b}$$

where we have used the definition $k = \langle R\rangle / R_c$ in the last step (*cf.* Eq. (1)). Here and in the following the brackets $\langle . \rangle$ denote the average over the aggregate assembly,

$$\langle f(R)\rangle := \frac{1}{N}\ \sum_i f(R_i) .$$

In particular, $\langle R\rangle$ is the average aggregate radius, and

$$\left\langle R^3\right\rangle = \frac{3V}{4\pi\, N} = 3\,\sigma D\ (k-1)\ t . \tag{4}$$

There is no constant term in this equation due to an appropriate choice of the initial time t_0 such that the initial volume V_0 amounts to

$$V_0 = \frac{4\pi}{3} \sum_i \left(R_i(t_0)\right)^3 = 4\pi\ \sigma D\ N_0\ (k-1)\, t_0 .$$

The linear growth ξ of the aggregate volume fraction $V/\mathcal{V}$ in a system of sample volume $\mathcal{V}$ amounts to

$$V = V_0 + \mathcal{V}\xi (t - t_0) . \tag{5a}$$

Together with Eq. (3b) this growth implies,

$$\mathcal{V}\xi := \dot{V} = 4\pi\ \sigma D\ N\ (k-1) \tag{5b}$$

such that we derive here the dependence anticipated in Eq. (1).

Altogether, we find the following set of equations for the evolution of the aggregate radii, R_i,

$$\dot{R}_i = \frac{\sigma D}{R_i^2}\ \left[k\ \frac{R_i}{\langle R\rangle} - 1\right] , \quad i = 1 \dots N , \tag{6}$$

where k is a function of the growth rate ξ, as stated in Eq. (1). The growth of the aggregate radii, R_i, is coupled in a mean-field way via the dependence of the equations on the average aggregate radius $\langle R\rangle$, and via k also explicitly on the number, $N = n\mathcal{V}$, of aggregates.

B. Numerical implementation

The implementation of the integration scheme is detailed in the flow chart provided in Fig. 2. To follow the size evolution of an assembly of aggregates, we integrate the cubes, $Q_i := R_i^3$ of their respective radii. This avoids instabilities in the numerics arising when directly integrating Eq. (6) for very small aggregates. In each time step we calculate the radii, R_i and their mean value, $\langle R\rangle$, and determine the updates of the Q_i via a predictor-corrector scheme that keeps track of the growth of the overall aggregate volume, Eq. (3b). It uses a recursion to identify and remove aggregates that evaporate in a given time step. Prior to calculating $\langle R\rangle$ and using Eq. (6) to determine the respective volume increments, the volume of evaporating aggregates is transferred to the volume increment to be added to the surviving aggregates.

All numerical data in the present paper refer to an initial assembly of N_0 aggregates with a distribution that is flat in the radius between $R = R_{\min} \dots R_{\max}$,

$$R_i = R_{\min} + (R_{\max} - R_{\min})\ \frac{i-1}{N_0 - 1} , \quad i = 1 \dots N_0 \tag{7a}$$

$$\text{with} \quad N_0 = 1000 , \quad R_{\min} = 0.02 , \quad R_{\max} = 3.00 . \tag{7b}$$

We make use of the linear growth of the overall aggregate volume, Eq. (5a), to specify the elapsed time in terms of the average aggregate volume, and choose the scale for the aggregate radius such that $\sigma D \equiv 1$.

For the bookkeeping of evaporation of aggregates we observe that the increasing order of the aggregate radius with index i is preserved by the evolution. After all, Eq. (6) implies that

$$Q_i > Q_j \Rightarrow \frac{\mathrm{d}}{\mathrm{d}t}(Q_i - Q_j) = \frac{3\sigma D\, k}{\langle R\rangle}\ (R_i - R_j) > 0 \tag{8}$$

such that the difference of the aggregate volumes grows strictly monotonously. Consequently, the evaporation of aggregates can conveniently be taken into account in our algorithm by appropriately truncating the range of the index i.

The algorithm admits adaptive step size control. After some testing we decided however to rather choose equidistant time steps on a logarithmic time axis because this saves the numerical overhead of the adaptive step size control and is convenient for the data analysis. For all data shown in this paper we

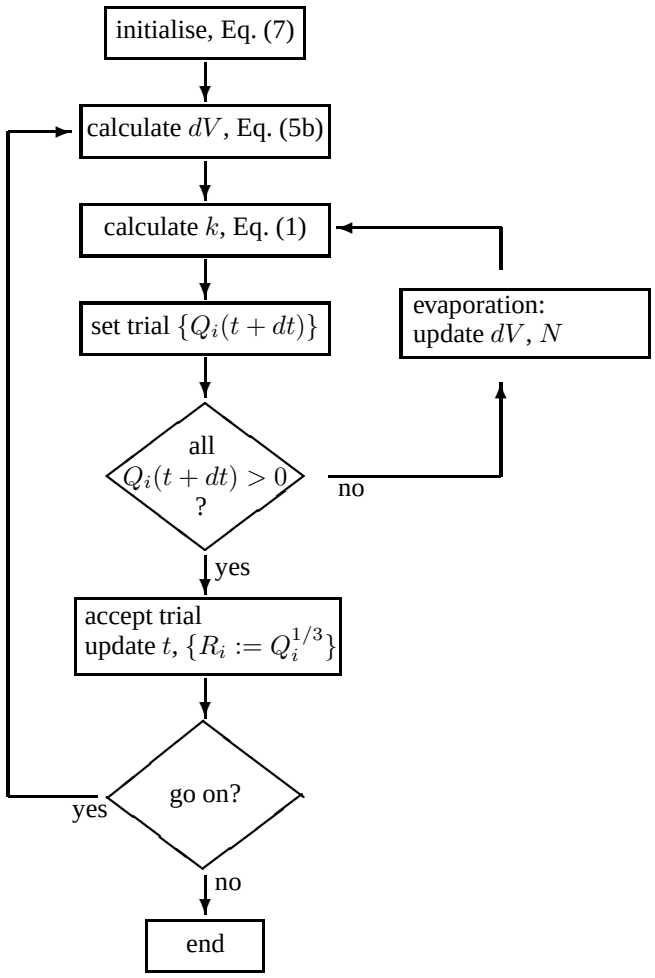

Figure 2 Schematics of the integration scheme for the size distribution $\{R_i\}_{i=1\ldots N}$, where the aggregate number N, the volume increments $\mathrm{d}V$ and the parameter k are self-consistently adjusted when small aggregates evaporate.

took 10^6 integration steps to increase the aggregate volume by one order of magnitude. This provides an accurate and very fast integration routine, where the simulation can span many orders of magnitude of aggregate growth.

Figure 3 shows the evolution of the cumulative aggregate size distribution (CDF), $\mathcal{C}(R)$, for four different values of ξ that correspond to initial values of $k = 5, 10, 50$, and 100. The CDF provides the fraction of aggregates with a radius smaller than R. Hence, for the flat initial distribution, Eq. (7), the initial CDF amounts to a function that rises linearly from zero at $R_{\min} = 0.02$ to one at $R_{\max} = 3.00$. This initial CDF is shown by the solid black line at the smallest values of R. To the right of this initial condition we show ten quadruples of functions displaying the respective CDFs at later times. Each set allows us to compare the shape of the CDF in a situation where the overall volume of the aggregates matches, *i.e.* for the same dimensionless time in our simulations. At this point we make four observation that we will be further substantiated in the forthcoming discussion:

- At early times the distributions for $k = 5$ and 10 develop a tail towards the small aggregates, and they feature larger average aggregate sizes at late times. This is a hallmark of the evaporation of aggregates. The tail is due to aggregates that shrink and evaporate when their radius approaches zero. The larger average size is required to achieve a prescribed overall volume with a smaller number of aggregates.
- The CDFs for $k = 50$ and 100 look almost the same. Indeed, this holds for all $k \gtrsim 50$, where no aggregates evaporate.
- From the inspection of the numerical data one verifies that for all $k > 1$ the growth at late times proceeds at a fixed aggregate number. Subsequently, the difference in shape with respect to the CDFs for larger values of k does not evolve any longer.
- All distributions become more and more monodisperse.

The evolution of the size of individual aggregates and their evaporation is discussed in Sec. IV.B, and in Sec. V we address the time evolution of the CDFs. These results rest upon a priori insights into the time evolution of the moments of the aggregate size distribution that are supplied in Sec. III.

III. MOMENTS OF THE AGGREGATE SIZE DISTRIBUTION

The set of differential equations (6) can be decoupled when the time evolution of N and $\langle R\rangle$ can be determined a priori, *i.e.* without explicitly integrating the set of equations $\dot{R}_i$. Our numerics revealed that for all $k > 1$ the number of aggregates N is constant at late times, and that for sufficiently large k there is no evaporation at all. In this section we therefore establish the time evolution of $\langle R\rangle$ for a constant number of aggregates, N.

A. Asymptotic evolution of $\langle R\rangle^2 \frac{\mathrm{d}}{\mathrm{d}t}\langle R\rangle$

For a constant number of particles the time derivative of the average aggregate radius

$$\langle R\rangle = \frac{1}{N}\,\sum_i R_i\,,$$

based on Eq. (6) is given by

$$\frac{\mathrm{d}}{\mathrm{d}t}\langle R\rangle = \frac{1}{N}\,\sum_i \dot{R}_i = \frac{1}{N}\,\sum_i \frac{\sigma D}{R_i^2}\,\left[k\,\frac{R_i}{\langle R\rangle} - 1\right] \quad \text{(9a)}$$

$$= \frac{\sigma D}{\langle R\rangle^2}\,\left[k\,\left\langle R^{-1}\right\rangle\,\langle R\rangle - \left\langle R^{-2}\right\rangle\,\langle R\rangle^2\right]\,. \quad \text{(9b)}$$

The products $\left\langle R^{-1}\right\rangle\langle R\rangle$ and $\left\langle R^{-2}\right\rangle\langle R\rangle^2$ eventually approach one because the size distribution becomes monodisperse in the long-time limit. Hence, in this limit the characteristic aggregate volume, $(4\pi/3)\,\langle R\rangle^3$, follows exactly the same law, Eq. (4), as the growth of the average aggregate volume $(4\pi/3)\,\left\langle R^3\right\rangle$,

$$\langle R\rangle^2\,\frac{\mathrm{d}}{\mathrm{d}t}\langle R\rangle = \sigma D\,(k-1) \quad \text{for large } t\,. \qquad (10)$$

This is demonstrated in Fig. 4 by showing that the ratio $\langle R\rangle^2\frac{\mathrm{d}}{\mathrm{d}t}\langle R\rangle/[\sigma D\,(k-1)]$ settles to one after some initial transient. In order to also understand the transient decay to the growth law, Eq. (10), we take a closer look at the difference of the time evolution of $\langle R\rangle^3$ and $\left\langle R^3\right\rangle$.

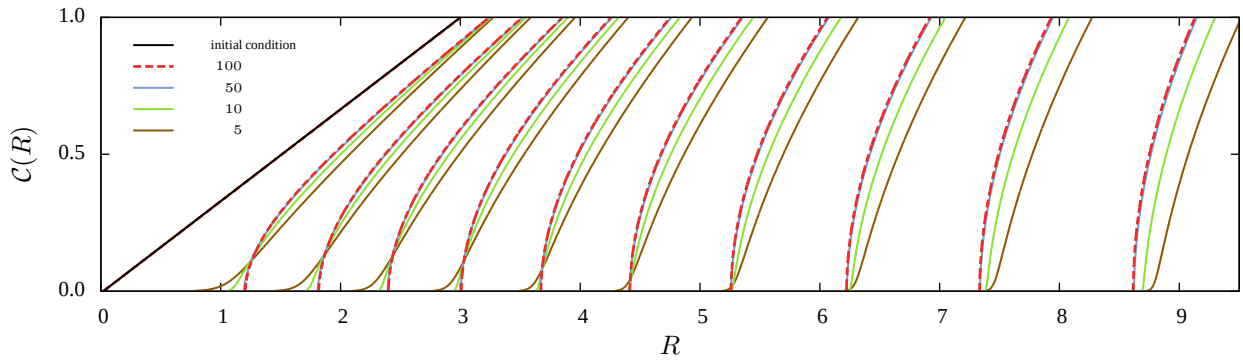

Figure 3 The four sets of curves of different colour show stroboscopic snapshots of the time evolution of the cumulative size distribution function, $\mathcal{C}(R)$, of aggregates for the same initial condition, and $k = 5$, 10, 50, and 100, respectively. Here and in the following we use dashed lines for the largest value of k displayed in the plot, and solid lines for all other curves. We use the same colour for all data referring to a given value of k, and provide the initial conditions, Eq. (7), by a solid black line (the leftmost curve). The time increments between successive curves of the same colour correspond to a time lapse resulting in an increase of the total aggregate volume by a factor of $10^{1/5}$. Consequently, the rightmost curves of each colour correspond to systems where the total aggregate volume grew by a factor of hundred. In the main text we discuss the similarities and differences between the CDFs in each of the resulting quadruplets. This allows us to pinpoint salient features of the impact of k on the time evolution of the CDFs.

B. Deviation of $\langle R\rangle^3$ from $\langle R^3\rangle$

Equations (4) and (10) state that in the long run the expectation values $\langle R\rangle^3$ and $\langle R^3\rangle$ acquire the same slope as functions of time. In order to gain insight into the difference of the two functions, we consider the expectation value $\langle R^4\rangle$.

We use $R = \langle R\rangle + (R - \langle R\rangle)$ and the forth power of this expression to observe that

$$\begin{aligned}\langle R^4\rangle - \langle R^2\rangle^2 &= -\left(\langle R^2\rangle + \langle R\rangle^2\right)\,\left\langle (R-\langle R\rangle)^2\right\rangle + 6\,\langle R\rangle^2\,\left\langle (R-\langle R\rangle)^2\right\rangle + 4\,\langle R\rangle\,\left\langle (R-\langle R\rangle)^3\right\rangle + \left\langle (R-\langle R\rangle)^4\right\rangle \\ &= 4\,\langle R\rangle^2\,\left\langle (R-\langle R\rangle)^2\right\rangle\,\left[1 + \frac{\left\langle (R-\langle R\rangle)^3\right\rangle}{\langle R\rangle\,\left\langle (R-\langle R\rangle)^2\right\rangle} + \frac{\left\langle (R-\langle R\rangle)^4\right\rangle}{4\,\langle R\rangle^2\,\left\langle (R-\langle R\rangle)^2\right\rangle} - \frac{\left\langle (R-\langle R\rangle)^2\right\rangle}{4\,\langle R\rangle^2}\right] \qquad (11)\end{aligned}$$

When approaching a monodisperse distribution the expression in square brackets rapidly approaches one, with corrections of order $\langle R\rangle^{-2}$. This observation provides the following insight into the leading order contributions to the difference $\langle R^3\rangle - \langle R\rangle^3$,

$$\left\langle R^3\right\rangle = \left\langle [\langle R\rangle + (R-\langle R\rangle)]^3\right\rangle \simeq \langle R\rangle^3 + 3\langle R\rangle\,\left\langle (R-\langle R\rangle)^2\right\rangle \simeq \langle R\rangle^3 + \frac{3}{4\,\langle R\rangle}\,\left\langle \left(R^2 - \langle R^2\rangle\right)^2\right\rangle$$

where we used Eq. (11) in the last step. Rearranging the equation yields

$$\langle R\rangle^3 = \langle R^3\rangle - \frac{3\Omega_2}{4\,\langle R\rangle} \qquad (12a)$$

$$\text{with} \qquad \Omega_2 = \left\langle \left(R^2 - \langle R^2\rangle\right)^2\right\rangle . \qquad (12b)$$

Numerical data shows that Ω_2 has a much weaker time dependence than $\langle R\rangle^{-1}$. Hence, the time derivative of Eq. (12a) amounts to

$$\langle R\rangle^2\,\frac{\mathrm{d}}{\mathrm{d}t}\langle R\rangle \simeq \sigma D\,(k-1) + \frac{\Omega_2}{4\,\langle R\rangle^4}\,\langle R\rangle^2\,\frac{\mathrm{d}}{\mathrm{d}t}\langle R\rangle$$

$$\Leftrightarrow \langle R\rangle^2\,\frac{\mathrm{d}}{\mathrm{d}t}\langle R\rangle = \sigma D\,(k-1)\,\left(1 - \frac{\Omega_2}{4\,\langle R\rangle^4}\right)^{-1} . \qquad (13a)$$

The dotted grey line in Fig. 4 shows the resulting prediction when one assumes that Ω_2 never noticeably deviates from its initial value

$$\Omega_2 = \frac{1}{5}\,\frac{R_{\max}^5 - R_{\min}^5}{R_{\max} - R_{\min}} - \left(\frac{1}{3}\,\frac{R_{\max}^3 - R_{\min}^3}{R_{\max} - R_{\min}}\right)^2 \qquad (13b)$$

determined for the initial aggregate size distribution, Eq. (7). For the specified values $R_{\max} = 3$ and $R_{\min} = 0.02$ it takes the value $\Omega_2 \simeq 7.19$. The inset of Fig. 4 shows the difference between this prediction and the numerical data. The strong fluctuation in the data for $k \lesssim 5$ are due to singularities in the evolution arising when an aggregate reaches zero radius. They reflect the evaporation of aggregates, and we will not apply Eq. (13) in that case since it was derived based on the assumption of no evaporation. On the other hand, for $k \gtrsim 5$ and $t - t_0 \gtrsim t_0$, *i.e.* once the overall aggregate volume has doubled, Eq. (13) provides an accurate description of the evolution.

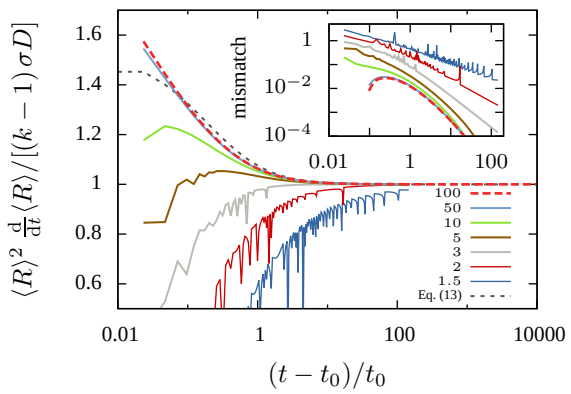

Figure 4 Evolution of $\langle R\rangle^2 \frac{\mathrm{d}}{\mathrm{d}t}\langle R\rangle$ for different values of k, as indicated in the legend. The data is obtained by evaluating Eq. (9b) for our numerical data. As predicted by Eq. (10) it always approaches $\sigma D\,(k-1)$ for large t. In the inset we show the mismatch of the numerical data and the improved prediction, Eq. (13).

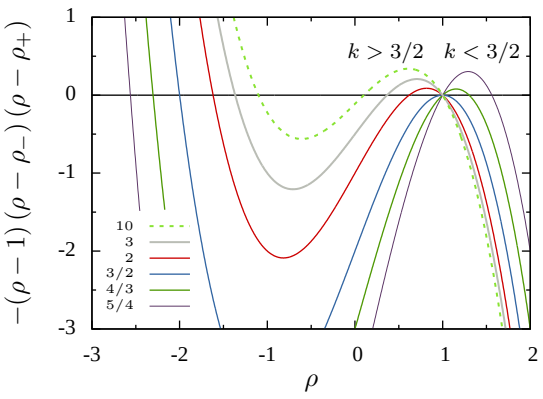

Figure 5 The cubic polynomial in the numerator of Eq. (16a). For all $k>1$ its three roots give rise to three fixed points of the reduced radius, ρ that are located at $\rho=1$ and $\rho=\rho_\pm$. For $k=3/2$ there is a bifurcation where the roots $\rho=1$ and ρ_+ change stability.

C. The variance of the distribution

Equations (11) and (12b) provide the variance of the aggregate size distribution

$$\left\langle \left(R-\langle R\rangle\right)^2 \right\rangle \simeq \frac{\Omega_2}{4\,\langle R\rangle^2}\,. \tag{14}$$

Remarkably, the standard deviation decays like $\langle R\rangle^{-1}$. Based on the approximation that the aggregate size distribution amounts to a Gaussian at all times this results has previously been obtained by Clark *et al.* (2011). However, in contrast to Eq. (14) these authors predicted a slightly different decay that scales like $\langle R\rangle^{-2+2/(k-1)}$. In Sec. V.B we will show that this discrepancy arises from a very slight time dependence of Ω_2: it increases like $\langle R\rangle^{2/(k-1)}$. For large k this correction is negligible such that it is not captured by the present analysis.

The central results of this section are Eqs. (10) and (13a). They express that one can accurately integrate the average radius $\langle R\rangle$ without need to refer to the evolution of the individual aggregates: the average $\langle R\rangle$ need not be calculated self-consistently as an average over the aggregates, but it has its own evolution equation, Eq. (13a). The solution of this equation explicitly solves the global constraint that couples the set of equations (6). Hence, the N dimensional system of non-linear coupled equations (6) for the aggregate radii R_i is reduced to N identical one-dimensional differential equations that only differ by their initial conditions. Henceforth, we concentrate on this equation and suppress the index i.

IV. THE REDUCED AGGREGATE RADIUS

The evolution of the decoupled set of equations (6) is most conveniently studied based on the reduced aggregate radius $\rho = R/\langle R\rangle$ that accounts for the trivial drift of the aggregate size due to the overall volume growth.

A. Equation of motion

Using Eq. (6) the time derivative of ρ can be written as

$$\begin{aligned}\dot\rho &= \frac{d}{dt}\frac{R}{\langle R\rangle} = \frac{\dot R}{\langle R\rangle} - \rho\,\frac{\frac{\mathrm{d}}{\mathrm{d}t}\langle R\rangle}{\langle R\rangle}\\ &= \frac{\sigma D}{\langle R\rangle\ R^2}\ [k\,\rho-1] - \rho\,\frac{\frac{\mathrm{d}}{\mathrm{d}t}\langle R\rangle}{\langle R\rangle}\\ &= -\frac{\sigma D}{\langle R\rangle^3}\,\rho^{-2}\left[\frac{\langle R\rangle^2\,\frac{\mathrm{d}}{\mathrm{d}t}\langle R\rangle}{\sigma D}\,\rho^3 - k\,\rho+1\right] \end{aligned}\tag{15}$$

According to Eq. (10) (or Fig. 4) the factor $\langle R\rangle^2\,\frac{\mathrm{d}}{\mathrm{d}t}\langle R\rangle/(\sigma D)$ approaches $k-1$ after a short initial transient. Consequently,

$$\begin{aligned}\dot\rho &\simeq -\frac{\sigma D}{\langle R\rangle^3}\,\frac{(k-1)\,\rho^3 - k\,\rho+1}{\rho^2}\\ &= -\frac{\sigma D\,(k-1)}{\langle R\rangle^3}\,\frac{(\rho-1)\ (\rho-\rho_-)\ (\rho-\rho_+)}{\rho^2}\end{aligned}\tag{16a}$$

with

$$\rho_\pm(k) = -\frac{1}{2} \pm \frac{1}{2}\,\sqrt{\frac{k+3}{k-1}}\,. \tag{16b}$$

The right-hand side of Eq. (16a) involves a cubic polynomial in ρ (Fig. 5). For all $k>1$ it gives rise to three fixed points of the reduced radius: the average aggregate radius $\rho=1$, a non-trivial radius ρ_+, and an unphysical fixed point ρ_- at negative values of ρ. Discussing their positions and stability for different reduced temperature ramp rates, Fig. 1, provides detailed insight into the dynamics.

$k=1$: We recover classical Ostwald ripening. The radius ρ_+ diverges, and the constraint on the overall aggregate volume gives rise to an asymptotic aggregate size distribution where the largest aggregates are of radius $\rho_{\max}=3/2$.

$1<k<3/2$: Eq. (16a) has an unstable fixed point at $\rho=1$, *i.e.* for $R=\langle R\rangle$. Aggregates that are smaller than the average radius shrink and they evaporate eventually

when they reach the radius $\rho = 0$. Aggregates larger than ρ_+ shrink, too, until they reach the stable aggregate radius ρ_+. On the other hand, aggregates in the range of $1 < \rho < \rho_+$ grow at the expense of the shrinking ones, also striving to reach the aggregate radius ρ_+. When all aggregates are smaller than ρ_+ and $\rho_+ \gg 3/2$ we expect a similar dynamic scaling theory to be applicable as the Lifshitz-Slyozov description of Ostwald ripening for $k = 1$ (see Slezov, 2009, for some pioneering work discussing this situation). In the following we concentrate on the case $k > 3/2$.

$k = 3/2$: The fixed points $\rho = 1$ and ρ_+ cross, and they exchange their stability. Beyond this value aggregate evaporation ceases wen all remaining aggregates have a size $\rho > \rho_+$.

$k > 3/2$: Eq. (16a) has a stable fixed point for $\rho = 1$, and an unstable fixed point at ρ_+ which rapidly approaches k^{-1} for $k \gtrsim 5$. After a brief initial transient no aggregates evaporate any longer, and the distribution becomes strongly peaked around the average aggregate radius $\langle R \rangle$. This is indeed what we have observed in Fig. 3.

B. Evaporation of aggregates

Aggregates that are smaller than $\langle R \rangle$ by a factor of ρ_+ shrink and evaporate when they reach zero size. For large values of k and reasonably smooth initial aggregate densities this can only be a small fraction of aggregates. Consequently, n does not change much when these aggregates disappear. To support this view we show in Fig. 6 that to an excellent approximation the number of aggregates bound to evaporate amounts to the number of aggregates in the initial distribution that lie below ρ_+.

The fate of a general initial distribution for an initial value of k in the range $1 < k \leq 3/2$ can be discussed based on Fig. 1. For $1 < k \leq 3/2$ the aggregates with a radius smaller than average shrink, and eventually they evaporate. While doing so the number density, n, decreases. According to Eq. (1) this results in an increase of k. This growth of k continues until all aggregates have a size $\rho > \rho_+$, *i.e.* their size lies above the the red line in Fig. 1. At that time k takes a value $k \gtrsim 3/2$, and in the subsequent long-time limit, k is a constant of motion.

For the initial conditions specified by Eq. (7) no aggregates should evaporate for $R_{\min}/\langle R \rangle > \rho_+(k_c) \simeq k_c^{-1}$, *i.e.* for $k_c > 75$. In practice, the numerical simulations show that k_c is slightly smaller. Systems subjected to a temperature ramp where $k > 64$, *i.e.* for $\xi \gtrsim 250\pi\sigma D\, n$ evolve at a constant number density, n, of aggregates, and hence at a constant value of k. When dealing with numerical data we always indicate the initial value of k, and self-consistently take into account its change in the plots. Our focus of attention will be the asymptotics of the shape of the aggregate size distribution.

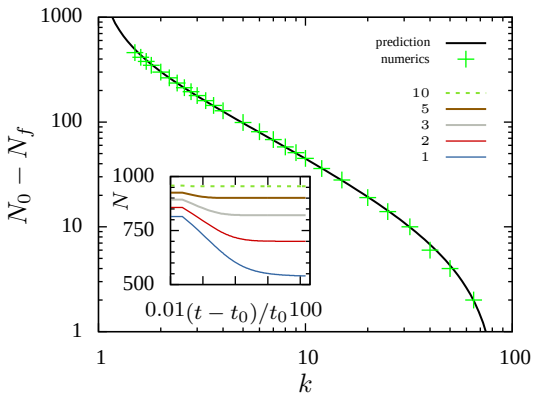

Figure 6 Evolution of the aggregate number. The inset shows the time evolution of the number of aggregates for different values of k. All systems are initialised with $N_0 = 1000$ aggregates with a size distribution as outlined in Eq. (7). Eventually, they settle down to a constant aggregate number, N_f. The main panel compares the number of evaporated aggregates $N_0 - N_f$ to the prediction that it should amount to $\int_0^{\rho_+} n(\varrho, t = t_0)\, \mathrm{d}\varrho$.

C. Evolution of the reduced aggregate radius

For all $k \gtrsim 3/2$ and sufficiently late times the evolution of the reduced aggregate radius, ρ, can be determined explicitly by integrating Eq. (15). Introducing the function

$$a = \langle R \rangle^3 / \left[3\sigma D\,(k-1)\right] \tag{17}$$

and focusing on values $\rho \simeq 1$ we write

$$\begin{aligned} 3\,(k-1)\,a\,\rho^2\,\dot\rho &= -(k-1)\,\dot a\,\rho^3 + (k-1)\rho + (\rho - 1) \\ &\simeq -(k-1)\,\rho\,\left[\dot a\,\rho^2 - 1\right] \end{aligned} \tag{18a}$$

$$\Leftrightarrow \qquad \frac{2}{3}\,a^{-1/3} = \frac{\mathrm{d}}{\mathrm{d}t}\left(a^{2/3}\rho^2\right)\,. \tag{18b}$$

This equation allows us to evaluate the derivative

$$\begin{aligned} \frac{\mathrm{d}}{\mathrm{d}t}R^2 &= \left[3\,\sigma D\,(k-1)\right]^{2/3}\,\frac{\mathrm{d}}{\mathrm{d}t}\left(a^{2/3}\,\rho^2\right) \\ &= \frac{2\,\sigma D\,(k-1)}{\langle R \rangle} \end{aligned} \tag{19a}$$

which agrees with the time derivative of $\langle R^2 \rangle$ up to a tiny correction

$$\begin{aligned} \frac{\mathrm{d}}{\mathrm{d}t}\langle R^2 \rangle &= \left\langle 2R\,\dot R \right\rangle \\ &= \frac{2\,\sigma D\,(k-1)}{\langle R \rangle}\,\left[1 + \frac{1 - \langle R \rangle\,\langle R^{-1} \rangle}{k-1}\right] \end{aligned} \tag{19b}$$

Altogether, Eqs. (19a) and (19b) imply that

$$\frac{\mathrm{d}}{\mathrm{d}t}\left(R^2 - \langle R^2 \rangle\right) = 0\,. \tag{20}$$

After all, there can be no merely time-dependent function appearing on the right-hand side of this equation because the expectation value $\langle R^2 - \langle R^2 \rangle \rangle$ must vanish at any time.

The result, Eq. (20), states that at late times aggregates always grow in such a way that the difference, $R^2 - \langle R \rangle^2$, is preserved. This has immediate implications on the aggregate size distribution which will be discussed in the next section.

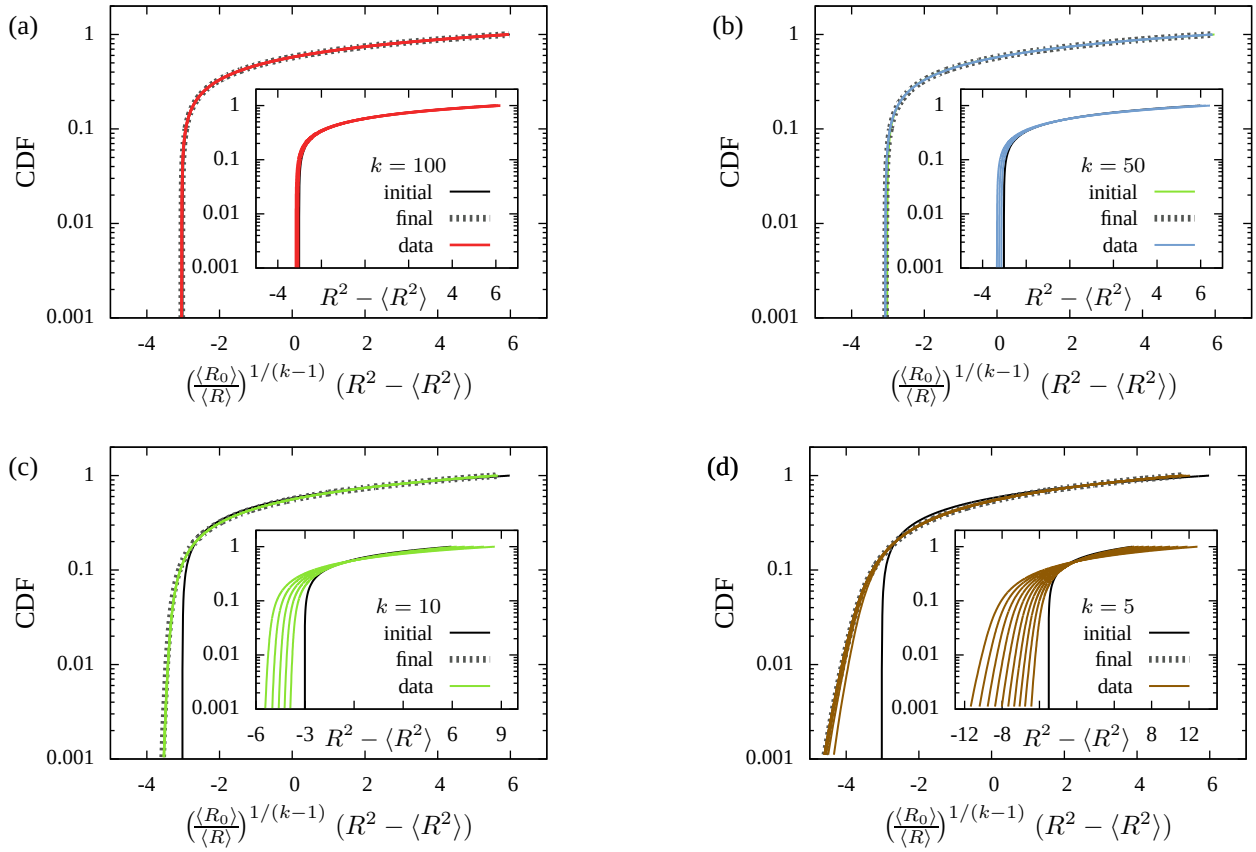

Figure 7 The CDFs (a) $k = 100$, (b) $k = 50$, (c) $k = 10$, and (d) $k = 5$. The insets show the CDFs as a function of $x = R^2 - \langle R^2 \rangle$ as suggested in Eq. (22), and the main panels the dependence on $\tilde{x}$ which has been defined in Eq. (30). The initial conditions are provided by solid black labelled by the tag "initial", and thin lines with colours matching those in Fig. 3 ("data") show the numerical results for a progression of time on a logarithmic scale. We provide here data where $\langle R \rangle$ grows to a size $\langle R \rangle \simeq 100$. As function of x the CDFs are slowly broadening in time (insets). As function of $\tilde{x}$ they approach an asymptotic distribution ("final") that is provided by dotted grey lines in the main panels.

V. EVOLUTION OF THE AGGREGATE SIZE DISTRIBUTION

According to Eq. (8) the order of the aggregate radii is preserved by the dynamics: when aggregate i is smaller than aggregate j initially, this holds also at all later times. Based on this observation and the explicit integration of the evolution equation of the aggregate radius, Eq. (20), one can derive the aggregate size distribution. This is most easily done based on the cumulative aggregate size distribution function (CDF).

A. Initial distribution, and its evolution based on Eq. (20)

For convenience of the discussion of the asymptotic shape of the CDF, we immediately remove the aggregates from the initial distribution that will evaporate. According to the arguments underpinned by Fig. 6 this amounts to the aggregates smaller than $R_c = \langle R_0 \rangle \ \rho_+(k)$, where $\langle R_0 \rangle = (R_{\rm max} + R_{\rm min})/2 = 1.51$ is the average radius with respect to the initial aggregate size distribution (7). When no aggregates evaporate we set $R_c = R_{\rm min}$. With this adoption, the CDF characterising the initial distribution, $\mathcal{C}(R_0)$, takes the form

$$\mathcal{C}(R_0) = \begin{cases} 0 & \text{for} \quad R_0 < R_c \,, \\ \frac{R_0 - R_c}{R_{\rm max} - R_c} & \text{for} \quad R_c < R_0 < R_{\rm max} \,, \\ 1 & \text{for} \quad R_{\rm max} < R_0 \,. \end{cases} \tag{21}$$

To avoid the involved notation required to explicitly distinguish the different branches of the function, we henceforth only specify its non-trivial branch, and keep in mind that the function should be set to zero when the expression drops below zero, and set to one when it rises beyond one.

In order to apply Eq. (20) it is convenient to rewrite Eq. (21) as a function of

$$x = R^2 - \left\langle R^2 \right\rangle \stackrel{!}{=} R_0^2 - \left\langle R_0^2 \right\rangle \,. \tag{22}$$

In that case the non-trivial branch of the CDF takes the form of a square-root dependence

$$\mathcal{C}(x) = \frac{\left[x + \left\langle R_0^2 \right\rangle\right]^{1/2} - R_c}{R_{\rm max} - R_c} \tag{23}$$

The initial condition $\mathcal{C}(x)$ of the CDF, provided as a function of x, is shown by solid black lines in Fig. 7(inset). To determine the time dependence of the CDF we note that according to Eq. (22) the value of x is preserved during the evolution. Consequently, the CDF should not change in time when it is

plotted as a function of x. To test this assertion the insets of Fig. 7 show the initial conditions together with the CDF at later times, that are shown in colours matching those used in Fig. 3. Except for the change of the variable, x rather than R, the CDFs shown in Fig. 3 and Fig. 7(inset) differ only by a different choice of the time increments. A larger factor of overall volume growth has been chosen in Fig. 7 in order to display distributions where the average radius grows to $\langle R\rangle \simeq 100$ rather than only till 9.

The prediction that the CDF remains invariant, Eq. (23), when plotted as a function of x properly captures main features of the time evolution: the CDFs fall on top of each other and they tend to preserve their form when plotted as a function of $x = R^2 - \langle R^2\rangle$. For all $k \gtrsim 50$ this provides an accurate description of the numerical data. On the other hand, for decreasing k the tails of the distributions towards the smaller aggregate sizes tend to become less steep, and in addition there is a noticeable broadening of the distributions in the course of time. These deviations arise from the fact that for $\rho \simeq 1$ we systematically underestimates the slope of $\dot\rho$ due to suppressing the term $(\rho-1)/(k-1)$ on the right hand side of Eq. (18a).

B. Accounting for broadening and shape changes

For late times, where Eq. (10) applies, we can gain insight into the broadening of the distribution by integrating Eq. (16) rather than Eq. (18).

We use Eq. (17) to write Eq. (16a) in the form

$$\dot\rho = -\frac{1}{3\,a}\frac{(\rho-1)\;(\rho-\rho_-)\;(\rho-\rho_+)}{\rho^2} \tag{24}$$

and introduce a function $g(\rho)$ that obeys the differential equation

$$\frac{\mathrm{d}g}{\mathrm{d}\rho} = \frac{\rho^2\, g}{(\rho-1)\;(\rho-\rho_-)\;(\rho-\rho_+)} \tag{25}$$

Combining Eqs. (24) and (25) allows us to rephrase the evolution of ρ in the form

$$\frac{\dot g}{g} = g^{-1}\,\frac{\mathrm{d}g}{\mathrm{d}\rho}\,\dot\rho = \frac{-1}{3\,a} = -\frac{\dot a}{3\,a}\,, \tag{26}$$

where we used in the last step that $\dot a = 1$ in the long-time asymptotics considered here. Equation (26) implies that

$$\frac{\mathrm{d}}{\mathrm{d}t}\left(g\;a^{1/3}\right) = 0\,. \tag{27}$$

In order to interpret this finding we have to find the function g. The differential equation (25) has solutions of the form

$$g = C\;(\rho-1)^{\alpha_1}\;(\rho-\rho_-)^{\alpha_-}\;(\rho-\rho_+)^{\alpha_+}\,, \tag{28a}$$

where the constant number C represents the integration constant. Inserting Eq. (28a) into Eq. (25) provides a linear set of equations for the exponents $(\alpha_1,\alpha_-,\alpha_+)$ that is solved by

$$\alpha_1 = \frac{1}{(2+\rho_+)\,(2+\rho_-)} = \frac{k-1}{2\,k-3}\,, \tag{28b}$$

$$\alpha_- = \frac{\rho_-^2}{(2+\rho_+)\;(1+2\rho_+)} \simeq \frac{1}{2} - \frac{1}{4k} + \frac{5}{8k^2} - \ldots \tag{28c}$$

$$\alpha_+ = \frac{\rho_+^2}{(2+\rho_-)\;(1+2\rho_-)} \simeq -\frac{1}{k^2} + \ldots\,, \tag{28d}$$

Equation (27) together with the definition of a, Eq. (17), entails that the cumulative distribution function is a function of $\langle R\rangle\, g$. Moreover, the insets of Fig. 7 show that in leading order of the long-time asymptotics, where $\langle R^2\rangle = \langle R\rangle^2$ (*cf.* Eq. (14)), the cumulative distribution function must depend on $R^2 - \langle R\rangle^2 = \langle R\rangle^2\,(\rho^2-1)$. This dependence can be faithfully recovered from $(\langle R\rangle\, g)^{1/\alpha_1}$ by observing that $\alpha_1^{-1} = 2 - (k-1)^{-1}$. Moreover, making use of $\alpha_1+\alpha_++\alpha_- = 1$ one easily shows that $\alpha_-/\alpha_1 = 1 - (k-1)^{-1} - \alpha_+/\alpha_1$. These relations provide

$$(\langle R\rangle\, g)^{\alpha_1^{-1}} = \langle R\rangle^{2-(k-1)^{-1}}\;(\rho^2-1)\;\left(1+\frac{\rho_+}{\rho+1}\right)\;(\rho+1+\rho_+)^{-(k-1)^{-1}}\;\left(\frac{\rho-\rho_+}{\rho+1+\rho_+}\right)^{\alpha_+/\alpha_1} \tag{29a}$$

$$\simeq \langle R\rangle^{-(k-1)^{-1}}\;\left(R^2-\langle R\rangle^2\right)\;\left[1+\mathcal{O}\big((k-1)^{-1}\big)\right]\,. \tag{29b}$$

The factor $\langle R\rangle^{-1/(k-1)}$ in Eq. (29b) entails that $\mathcal{C}(R^2-\langle R^2\rangle)$ features a sustained broadening, as observed for the CDFs shown in the insets of Fig. 7. In line with the k dependence of this factor the broadening is increasingly more pronounced for smaller values of k. In contrast the CDFs should remain invariant when accounting of the broadening by plotting $\mathcal{C}$ as a function of

$$\tilde x = \left(\frac{\langle R_0\rangle}{\langle R\rangle}\right)^{(k-1)^{-1}}\;\left(R^2-\langle R^2\rangle\right) \tag{30}$$

This variable accounts for the sustained broadening of the CDF via the factor $\langle R\rangle^{-1/(k-1)}$, and at early times it appropriately fixes the mean position of the CDF, as observed in Eq. (22).

The data collapse of the CDFs shown in the main panels of Fig. 7(a) and (b) demonstrates that for $k \gtrsim 50$ the CDFs are invariant when plotted as a function of $\tilde x$. For smaller values of k the variable $\tilde x$ faithfully accounts for the broadening of the distribution that was severely underestimated previously. However, the higher-order corrections specified by

the last three factors in Eq. (29a) affect the relation between $R^2 - \langle R^2 \rangle$ and its initial value $R_0^2 - \langle R_0^2 \rangle$ such that the shape of the distribution is no longer be preserved (Fig. 7(c) and (d)). The dotted grey lines show the shape of the distribution that results when these factors are accounted for. Taking into account these terms provides a parameter free prediction of the asymptotic form of the CDF that is accurate for all considered values of k.

C. Scaling of the centred moments of the size distribution

The observation that the aggregate size distribution is invariant when plotted as a function of $\tilde{x}$ has immediate consequences for the centred moments of the size distribution function. The data collapse implies that $\langle \tilde{x}^n \rangle$ is invariant in time such that

$$\Omega_n := \left\langle \left(R^2 - \langle R^2 \rangle \right)^n \right\rangle \sim \left(\frac{\langle R \rangle}{\langle R_0 \rangle} \right)^{n/(k-1)} . \qquad (31)$$

For small k the factor $\langle R \rangle^{2/(k-1)}$ provides a small, but noticeable growth of Ω_2 that is reflected in the broadening of the distributions shown in the insets of Fig. 7.

In order to calculate the centred moments we note that

$$R - \langle R \rangle = \frac{\left(R^2 - \langle R^2 \rangle \right) - \left(R - \langle R \rangle \right)^2 + \left\langle \left(R - \langle R \rangle \right)^2 \right\rangle}{2\langle R \rangle}$$

$$= \frac{1}{2\langle R \rangle} \left[\left(R^2 - \langle R^2 \rangle \right) + \mathcal{O}\left(\langle R \rangle^{-2} \right) \right]$$

Consequently,

$$\langle \left(R - \langle R \rangle \right)^n \rangle \simeq \left\langle \left(\frac{R^2 - \langle R^2 \rangle}{2 \langle R \rangle} \right)^n \right\rangle = \frac{\Omega_n}{\left(2 \langle R \rangle \right)^n}$$

In view of the asymptotic scaling, Eq. (31), of Ω_n this implies

$$\langle \left(R - \langle R \rangle \right)^n \rangle \sim \langle R \rangle^{-n+n/(k-1)} . \qquad (32)$$

In particular, we hence obtain the result anticipated in Sec. III.C: the standard deviation of the aggregate size distribution decays like

$$\sqrt{\langle R^2 \rangle - \langle R \rangle^2} = \frac{{\Omega_2}^{1/2}}{2 \langle R \rangle} \sim \langle R \rangle^{-1+(k-1)^{-1}} . \qquad (33)$$

VI. DISCUSSION

The data collapse achieved in Fig. 7 and the resulting scaling, Eq. (33), of the standard deviation of the size distribution underpin the assertion of Sec. III that the aggregate size distribution tends to become monodisperse when aggregates grow in an environment that leads to a sustained growth in their net volume. For all $k \gtrsim 5$ we have provided a scaling form of the asymptotic shape of the size distribution, and for $k \gtrsim 50$ the initial condition is described so faithfully by this scaling form that we have obtained a parameter-free prediction for all times. In order to digest the relevance of these findings it is important to estimate the order of magnitude of k for different processes.

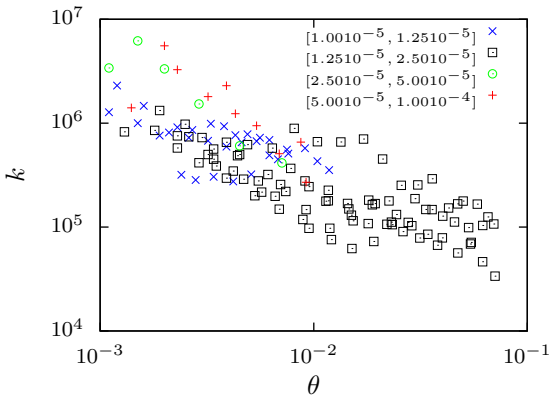

Figure 8 The k-values for the water-rich phase of the water/iso-butoxyethanol mixture as a function of the reduced temperature $\theta = (T - T_c)/T_c$ where $T_c = 25.5°\mathrm{C}$ is the critical temperature of the mixture. Different symbols refer to measurements where the volume-fraction growth rates, ξ, take values in the intervals indicated in the legend of the plot. The values of k have be calculated based on number densities n reported by Lapp *et al.* (2012), and the other material parameter are extrapolations of the respective parameters in literature which have been collected by Lapp (2011).

A. Optical and calorimetric measurements on the phase separation of binary mixtures

In a recent study Lapp *et al.* (2012) determined the evolution of the number density, n, of droplets in the phase separation of water/iso-butoxyethanol mixtures subjected to temperature protocols that lead to a constant growth of the droplet volume fraction. The ramp rates ξ of the increase of droplet volume fraction ranged from $\xi = 10^{-5}$ to 10^{-4} s^{-1}. Based on the temperature dependence of the pertinent material parameters (Lapp, 2011) we show in Fig. 8 that in those studies k took values in the range of $10^4 \ldots 10^7$. The wide range of k values results from exploring a range of ramp rates ξ that covers one order of magnitude, and from the temperature dependence of the material parameters.

Studies on other binary mixtures have observed phase separation during a slow temperature ramp in differential scanning micro-calorimetry (Auernhammer *et al.*, 2005; Heimburg *et al.*, 2000) or by optical measurements (Auernhammer *et al.*, 2005; Rullmann and Alig, 2004). These experiments typically involve gradual changes of the temperature T by about 1 K/h, which amounts to ξ in the range also explored by (Lapp *et al.*, 2012). Hence, we expect that they involve similarly large values of k.

B. Growth of cloud droplets

Rain emerges when the air masses in a cloud rise due to topographic constraints, or by encountering a cold front (Mason, 1971; Rogers and Yau, 1989). The drop of pressure in response to the rising of height H leads to adiabatic cooling of the air. This in turn changes the solubility of water in the air. Similarly to the phase separation discussed in Sec. VI.A this induces a continuous growth of cloud droplets until they reach a size where collisions due to gravity and inertia speed up their growth and trigger rain formation (Bodenschatz *et al.*, 2010).

T [°C]	-40	0	10
$\mathrm{d}\Phi/\mathrm{d}T$ [K^{-1}]	$2 \cdot 10^{-5}$	$4.5 \cdot 10^{-4}$	$8 \cdot 10^{-4}$
ξ [s^{-1}]	$2 \cdot 10^{-7}$	$4.5 \cdot 10^{-6}$	$8 \cdot 10^{-6}$
γ [N/m]	$8.4 \cdot 10^{-2}$	$7.6 \cdot 10^{-2}$	$7.4 \cdot 10^{-2}$
Φ	$1.9 \cdot 10^{-4}$	$6.1 \cdot 10^{-3}$	$1.2 \cdot 10^{-2}$
k	8.0	5.7	5.2

Table I Material constants for mixtures of water and air, and the resulting values for ξ and k based on a vertical wind speed of $\mathrm{d}H/\mathrm{d}t = 1$ m/s. Values for other wind speeds can easily be obtained by observing that $k-1$ is proportional to $\mathrm{d}H/\mathrm{d}t$.

Clement (2009) discussed the micro-physics of the droplet growth, emphasising the importance of the heat of condensation and the impact of solutes in the droplets.

Here we augment his study by an estimate of the possible impact of the continuous growth of the droplet volume fraction. We note that ξ amounts to the product of three factors,

$$\xi = \frac{\mathrm{d}\Phi}{\mathrm{d}t} = \frac{\mathrm{d}\Phi}{\mathrm{d}T}\,\frac{\mathrm{d}T}{\mathrm{d}H}\,\frac{\mathrm{d}H}{\mathrm{d}t}\,,$$

where $\Phi = V/\mathcal{V}$ is the volume fraction of droplets. The three factors on the right hand side of the equation amount to the slope of the phase boundary,[1] $\mathrm{d}\Phi/\mathrm{d}T \lesssim 5 \cdot 10^{-4}\ \mathrm{K}^{-1}$ (Moran and Morgan, 1997, p. 132), the adiabatic lapse rate $\mathrm{d}T/\mathrm{d}H \simeq 1\,\mathrm{K}/100\,\mathrm{m}$ ((Moran and Morgan, 1997, p. 148) or (Rogers and Yau, 1989, p. 29)), and the average upwind speeds, $\mathrm{d}H/\mathrm{d}t = 1 \ldots 10$ m/s, respectively. This gives rise to values of ξ between $5 \cdot 10^{-6}\mathrm{s}^{-1}$ and $5 \cdot 10^{-5}\mathrm{s}^{-1}$.

The number density of droplets in a cloud has been determined by Ditas *et al.* (2012) in recent measurement campaigns, $n = 4.7 \cdot 10^{8}\mathrm{m}^{-3}$, and the values of the diffusion constant and the Kelvin length are well-known material constants. The latter is obtained by inserting the values of the interfacial tension of the water-air interface, γ, the molar volume of liquid water, $V_m = 18 \cdot 10^{-6}\mathrm{m}^3/\mathrm{mol}$, (Mason, 1971, p. 614), the equilibrium volume faction of water vapour in air, Φ, the molar gas constant, $R = 8.3$ J/mol K, and the temperature T into the definition of the Kelvin length (Landau and Lifshitz, 1983)

$$\sigma = \frac{2\,\gamma V_m \Phi}{RT}\,. \tag{34}$$

In Table I we provide some representative data and the resulting values for ξ and k. For average vertical wind speeds of 1 m/s the values of k lie in the range of $5 \ldots 8$, and for larger wind speeds higher values are obtained.

We stress that the values provided in Table I provide only a rough, first order estimate of the parameters governing the evolution of the droplet size distribution in clouds. Nevertheless, this estimate suggests that the droplet volume growth due to the average rising of a cloud can give rise to values of k in the range, $k \gtrsim 5$ where the present results promise the arising of interesting new physics. This calls for a careful revisiting of the pertinent droplet growth laws.

[1] It has been demonstrated by Lapp *et al.* (2012) that $\mathrm{d}\Phi/\mathrm{d}T$ amounts to the slope of the binodal line of the phase diagram.

T [°C]	40	50	60	70
D [m^2/s]	$9.94 \cdot 10^{-10}$	$1.26 \cdot 10^{-9}$	$1.56 \cdot 10^{-9}$	$1.92 \cdot 10^{-9}$
C_∞ [$\frac{\mathrm{mol}}{\mathrm{m}^3}$]	$1.01 \cdot 10^{-4}$	$2.12 \cdot 10^{-4}$	$4.34 \cdot 10^{-4}$	$8.42 \cdot 10^{-4}$
N	$3.20 \cdot 10^{17}$	$1.25 \cdot 10^{17}$	$4.60 \cdot 10^{16}$	$2.20 \cdot 10^{16}$
k	1.63	1.62	1.69	1.62

Table II Representative material parameters for the synthesis of monodisperse Ag Br particles (adapted from Sugimoto, 1992) and the corresponding k values as calculated via Eqs. (35). The molar volume of Ag Br is $V_m = 2.9 \cdot 10^{-5}\mathrm{m}^3/\mathrm{mol}$, and its specific surface energy is $\gamma = 1.77 \cdot 10^{-1}\mathrm{J/m}^2$. All experiments were conducted with a mass supply rate, $Q_0 = 10^{-3}\mathrm{mol/s}$.

C. Synthesis of monodisperse colloids and nano-particles

Fundamental work on the synthesis of monodisperse colloids goes back to LaMer and Dinegar (1950) and Reiss (1951). The theoretical understanding of the mechanisms that lead to highly monodisperse colloids and nano-crystals is still a topic of active research (Clark *et al.*, 2011; Rempel *et al.*, 2009; Singh *et al.*, 2012).

For the synthesis of monodisperse silver particles (used for photographic films) the material flux is well defined, and all material constants required to determine the k-values have been documented. For the synthesis of Ag Br and Ag Cl particles Sugimoto (1992) and Sugimoto *et al.* (2000) provide material constants and aggregate numbers that allow us to calculate k based on the increase of the total volume of the aggregates, $\xi\mathcal{V}$, the diffusion coefficient D, and the Kelvin length σ,

$$k = 1 + \frac{\xi}{4\pi D\sigma n} = 1 + \frac{Q_0 V_m}{4\pi D\sigma N}\,, \tag{35a}$$

where N is the number of aggregates in the sample volume $\mathcal{V}$, and

$$\xi = V_m\, Q_0/\mathcal{V} \tag{35b}$$

is provided in terms of the molar volume, V_m, and the mass supply rate, Q_0. Finally, the specific surface energy γ, the buffer temperature T, the mean-field monomer concentration C_∞, and the molar gas constant $R = 8.314$ J/(mol K) provide the Kelvin length as

$$\sigma = \frac{2\gamma V_m^2 C_\infty}{RT}\,. \tag{35c}$$

Table II provides the resulting k-values for different representative sets of (T, D, C_∞, N) used for the synthesis of Ag Br particles, and Table III provides the k values for the synthesis of Ag Cl particles. Also in the latter case the k values are obtained from Eqs. (35), except that Sugimoto *et al.* (2000) provided the molar injection rate $q_0 = Q_0/\mathcal{V}$ and the number density of particles, $n = N/\mathcal{V}$.

The data show that the k values selected for the synthesis of monodisperse silver particles lie at $k \simeq 1.6$ for Ag Br-particles and in a range between 6 and 43 for Ag Cl. Moreover, for the initial stages of the synthesis of Ce Sd nanocrystals Clark *et al.* (2011) estimated k to lie in the range of $k \simeq 3 \ldots 5$ (see their Fig. 4). These choices have been obtained by tuning the temperature and the rates Q_0 or q_0 for optimal monodispersity of the product. In all cases this resulted

in k values larger than $3/2$ such that one can profit from the size focusing arising for $k > 3/2$. In principle, the values of k should be chosen as large as possible to achieve the smallest standard deviation, Eq. (33), and minimise the time required for the synthesis, Eq. (4). In practice, it becomes harder to realise stable and reproducible experimental conditions for large values of k, and the heat released in the growth might severely alter the present theory for large growth rates. Follow-up work will have to explore these effects.

VII. CONCLUSION

In Eqs. (1) we have identified the dimensionless factor k as control parameter determining the features of the evolution of an aggregate distribution evolving with overall volume growth. For $k = 1$ (*i.e.* no growth) the dynamics recovers the Lifshitz-Slyozov-Wagner scenario of Ostwald ripening (Bray, 1994; Voorhees, 1985). For $1 < k < 3/2$ we expect Ostwald-like behaviour as described by Slezov (2009, Chap. 7). In the present paper we focused on the case $k > 3/2$. On the one hand, we established a new numerical algorithm, that is outlined in Fig. 2. It allows us to accurately follow the evolution of the aggregate size distribution over very long times because it admits equidistant time stepping on a logarithmic time axis. On the other hand, we have provided a complete analytical solution for the evolution of the aggregate size distribution. It has no adjustable parameters and agrees perfectly with the numerical data.

This excellent agreement establishes that for $k > 3/2$ the CDF does not approach a scaling form. Rather it is most conveniently written as a function of the difference, $R^2 - \langle R^2 \rangle$, of the square of the considered radius, R, and its average, $\langle R^2 \rangle$. We demonstrated in Fig. 7 that to a very good approximation the shape of the distribution function remains invariant when this dependence is augmented by a gradual broadening by a factor $\langle R \rangle^{1/(k-1)}$. Sub-dominant contributions to the evolution can arise from small aggregates that grow slightly slower than those of average size. They lead to noticeable changes in the small-size tail of the distribution for $k \lesssim 10$. The resulting change of the shape of the distribution can be accounted for by considering the higher order correction in Eq. (29a) and by self-consistently tracking the influence of the evaporation of aggregates. The resulting parameter-free prediction provides an excellent description of the asymptotic shape of the distribution (dotted grey lines in Fig. 3). Consequently, the shape of the aggregate size distribution is fully determined by its initial condition, rather than by features of the dynamics.

In conclusion we have established that a weak thermal drift, or any other mechanism that leads to slow aggregate growth, can have dramatic effects on the aggregate size distribution. Even for very small effective driving it has a noticeable impact on various features of the aggregate size distribution.

The **aggregate number density** is constant at late times (see Fig. 6). In contrast to this finding for $k > 1$, the ripening in isothermal systems (*i.e.* for $k = 1$) can only evolve by evaporation of small aggregates. This leads to a t^{-1} decay of the number of aggregates.

The **mean aggregate radius** grows like $\langle R \rangle \sim t^{1/3}$. In contrast to Ostwald ripening, this growth is not connected to the evaporation of aggregates, but reflects the growth due to a constant volume flux onto the aggregates at a fixed number of aggregates.

The **standard deviation of the aggregate radius** decays with the non-trivial power $(t^{1/3})^{-1+1/(k-1)}$ (*cf.* Eq. (33)). Consequently, the relative width of the distribution, which amounts to the ratio of the standard deviation and the average radius, $\langle R \rangle$, decays like $(t^{1/3})^{-2+1/(k-1)}$. The aggregate size distribution tends to become more and more monodisperse.

The **shape of the distribution** is governed by initial conditions, rather than being universal. When plotted as a function of $\tilde{x}$ specified by Eq. (30) the cumulative distribution function remains invariant except for small k where there is a slight change of the tails. It has been accounted for in the theoretical prediction shown by the dotted grey lines in Fig. 7.

T [°C]	25	30	35	40
D [m^2/s]	$1.44 \cdot 10^{-9}$	$1.64 \cdot 10^{-9}$	$1.86 \cdot 10^{-9}$	$2.11 \cdot 10^{-9}$
C_∞ [$\frac{\text{mol}}{\text{m}^3}$]	$5.04 \cdot 10^{-4}$	$7.30 \cdot 10^{-4}$	$1.04 \cdot 10^{-3}$	$1.46 \cdot 10^{-3}$
n[m^{-3}]	$5.88 \cdot 10^{13}$	$5.71 \cdot 10^{13}$	$4.24 \cdot 10^{13}$	$2.70 \cdot 10^{13}$
q_0 [$\frac{\text{mol}}{\text{m}^3\text{s}}$]	$5.95 \cdot 10^{-6}$	$1.54 \cdot 10^{-5}$	$3.86 \cdot 10^{-5}$	$8.88 \cdot 10^{-5}$
ξ [s^{-1}]	$1.54 \cdot 10^{-10}$	$3.99 \cdot 10^{-10}$	$1.00 \cdot 10^{-9}$	$2.30 \cdot 10^{-9}$
k	6.26	9.64	19.4	43.3

Table III Material parameters for the synthesis of monodisperse Ag Cl particles (adapted from Sugimoto *et al.*, 2000, table 3), and the resulting k-values as calculated via Eqs. (35). For Ag Cl particles the molar volume is $V_m = 2.59 \cdot 10^{-5}$m^3/mol, and their specific surface energy is $\gamma = 1.009 \cdot 10^{-1}$J/m^2.

The latter two findings are in striking contrast to those of the Lifshitz-Slyozov-Wagner theory of Ostwald ripening, which predicts that the distribution approaches a universal distribution with a fixed relative width.

For a range of different applications we have demonstrated in Sec. VI that values of $k > 3/2$, where these differences prominently apply, may be regarded as common rather than as an exception. Consequently, the theory for the aggregate size distributions, that we have established in Sec. V, opens new opportunities in the characterisation and synthesis of aggregate growth. On the one hand, one can use the growth as a microscope to infer the initial size distribution at nucleation from a measurement at a later time when the aggregates have grown to a larger size. On the other hand, the distinct dependence of the size distribution on the initial conditions can be exploited to generate assemblies of aggregates with tailored size distributions. Moreover, in situations where k shows a non-trivial evolution in time the present theory provides a more natural starting point for an analysis of the aggregate growth than the Lifshitz-Slyozov-Wagner theory, because according to Eq. (1) the point $k = 1$ is unstable with respect to growth of k when n decreases due to the evaporation of aggregates.

ACKNOWLEDGMENTS

We acknowledge feedback by Karl-Henning Rehren upon developing the present theory, and inspiring discussions with Markus Abel, Bernhard Altaner, Nicolas Rimbert, Artur Wachtel, and Michael Wilkinson. Lucas Goehring, Stephan Herminghaus, and Artur Wachtel provided feedback on the manuscript.

REFERENCES

Auernhammer, Günter K, Doris Vollmer, and Jürgen Vollmer (2005), "Oscillatory instabilities in phase separation of binary mixtures: Fixing the thermodynamic driving," J. Chem. Phys. **123**, 134511.

Barenblatt, Grigory I (2003), *Scaling*, Cambridge Texts in Applied Mathematics (Cambridge UP, Cambridge, New York).

Bodenschatz, Eberhard, Szymon P. Malinowski, Raymond A. Shaw, and Frank Stratmann (2010), "Can we understand clouds without turbulence?" Science **327**, 970–971.

Bray, Alan J (1994), "Theory of phase-ordering kinetics," Adv. Phys. **43**, 357 – 459.

Cates, Michael E, Jürgen Vollmer, Alexander Wagner, and Doris Vollmer (2003), "Phase separation in binary fluid mixtures with continuously ramped temperature," Phil. Trans. Roy. Soc. (Lond.) Ser. A **361**, 793–807, cond-mat/0304085.

Clark, Michael D, Sanat K. Kumar, Jonathan S. Owen, and Emory M. Chan (2011), "Focusing nanocrystal size distributions via production control," Nano Lett. **11**, 1976–1980.

Clement, Charles F (2009), "Mass transfer to aerosols," in *Environmental Chemistry of Aerosols*, edited by Ian Colbeck (Blackwell Publishing Ltd., Oxford) pp. 49–89.

Ditas, Florian, Raymond A. Shaw, Holger Siebert, Martin Simmel, Birgit Wehner, and Alfred Wiedensohler (2012), "Aerosols-cloud microphysics-thermodynamics-turbulence: evaluating supersaturation in a marine stratocumulus cloud," Atm. Chem Phys. **12** (5), 2459–2468.

Goudon, Thierry, Frédéric Lagoutiére, and Léon M. Tine (2012), "The Lifschitz-Slyozov equation with space-diffusion of monomers," Kinetic and related models **5** (2), 325 – 355.

Han, Weon S, M. Lu, B. J. McPherson, E. H. Keating, J. Moore, E. Park, Z. T. Watson, and N.-H. Jung (2013), "Characteristics of CO_2-driven cold-water geyser, crystal geyser in Utah: experimental observation and mechanism analyses," Geofluids **13** (3), 283–297.

Heimburg, Thomas, Sirojiddin Z. Mirzaev, and Udo Kaatze (2000), "Heat capacity behavior in the critical region of the ionic binary mixture ethylammonium nitrate—n-octanol," Phys. Rev. E **62**, 4963–4967.

Ingebritsen, S E, and S. A. Rojstaczer (1993), "Controls on geyser periodicity," Science **262** (5135), 889–92.

Jana, Santanu, Bhupendra B. Srivastava, and Narayan Pradhan (2013), "A controlled growth process to design relatively larger size semiconductor nanocrystals," J. Phys. Chem. C **117** (2), 1183–1188.

Johnson, Noah J J, Andreas Korinek, Cunhai Dong, and Frank C. J. M. van Veggel (2012), "Self-focusing by Ostwald ripening: A strategy for layer-by-layer epitaxial growth on upconverting nanocrystals," J. Am. Chem. Soc. **134** (27), 11068–11071.

Kahlweit, Manfred (1976), "On the kinetics of precipitation," Faraday Disc. **61**, 48 – 52.

Kwon, Soon Gu, and Taeghwan Hyeon (2011), "Formation mechanisms of uniform nanocrystals via hot-injection and heat-up methods," Small **7** (19), 2685–2702.

LaMer, Victor K, and Robert H. Dinegar (1950), "Theory, production and mechanism of formation of monodispersed hydrosols," J. Am. Chem. Soc. **72** (11), 4847–4854.

Landau, Lev D, and Evgeny M. Lifshitz (1983), *Lehrbuch der theoretischen Physik*, Vol. X. Physikalische Kinetik (Akademie, Berlin).

Lapp, Tobias (2011), *Evolution of Droplet Distributions in Hydrodynamic Systems*, Ph.D. thesis (Georg August University Göttingen – Göttingen Graduate School for Neurosciences, Biophysics, and Molecular Biosciences).

Lapp, Tobias, Martin Rohloff, Jürgen Vollmer, and Björn Hof (2012), "Particle tracking for polydisperse sedimenting droplets in phase separation," Exp. Fluids **52**, 1187–1200.

Lifshitz, Ilya M, and Vitaly V. Slyozov (1961), "The kinetics of precipitation from supersaturated solid solutions," J. Phys. Chem. Solids **19** (1–2), 35 – 50.

Ludwig, Frank-Peter, and Jürn Schmelzer (1995), "Cluster formation and growth in segregation processes with constant rates of supply of monomers," Z. Phys. Chem. **192** (2), 155 – 167.

Manga, Michael (1996), "Waves of bubbles in basaltic magmas and lavas," J. Geophys. Res.: Solid Earth **101** (B8), 17457–17465.

Martin, Daniel, and Roger Nokes (1988), "Crystal settling in a vigorously converting magma chamber," Nature **332**, 534 – 536.

Mason, Basil J (1971), *The Physics of Clouds*, 2nd ed., Oxford Monographs on Meterology (Oxford University Press).

Moran, Joseph H, and Michael D. Morgan (1997), *Meteorolgy: The Atmosphere and the Science of Weather*, 5th ed. (Prentice-Hall).

Niethammer, Barbara, and Robert L. Pego (1999), "Non-self-similar behavior in the LSW theory of Ostwald ripening," J. Stat. Phys. **95** (5–6), 867–902.

Nozawa, Koh, Marie-Hélène Delville, Hideharu Ushiki, Pascal Panizza, and Jean-Pierre Delville (2005), "Growth of monodisperse mesoscopic metal-oxide colloids under constant monomer supply," Phys. Rev. E **72**, 011404.

Ostwald, Wilhelm (1900), "Über die vermeintliche Isomerie des roten und gelben Quecksilberoxyds und die Oberflächenspannung fester Körper," Z. phys. Chem. **34**, 495 – 503.

Peng, Xiaogang, J. Wickham, and A. P. Alivisatos (1998), "Kinetics of II–VI and III–V colloidal semiconductor nanocrystal growth: "focusing" of size distributions," J. Am. Chem. Soc. **120**, 5343.

Penrose, Oliver (1997), "The Becker-Döring equations at large times and their connection with the LSW theory of coarsening," J. Stat. Phys. **89**, 305 – 320.

Reiss, Howard (1951), "The growth of uniform colloidal dispersions," J. Chem. Phys. **19** (4), 482 – 487.

Rempel, Jane Y, Moungi G. Bawendi, and Klavs F. Jensen (2009), "Insights into the kinetics of semiconductor nanocrystal nucleation and growth," J. Am. Chem. Soc. **131** (12), 4479 – 4489.

Rogers, Roddy R, and M. K. Yau (1989), *A Short Course in Cloud Physics*, 3rd ed., International Series in natural philosophy, Vol. 113 (Pergamon Press, Oxford).

Rullmann, Max, and Ingo Alig (2004), "Scaling behavior of nonisothermal phase separation," J. Chem. Phys. **120**, 7801–7810.

Shneidman, Vitaly A (2013), "Early stages of Ostwald ripening," Phys. Rev. E **88**, 010401.

Singh, Awaneesh, Sanjay Puri, and Chandan Dasgupta (2012), "Growth kinetics of nanoclusters in solution," J. Phys. Chem. B **116** (15), 4519–4523.

Slezov, Vitaly V (2009), *Kinetics of First-Order Phase Transitions* (Wiley-VCH, Weinheim).

Smereka, Peter (2008), "Long time behavior of a modified Becker-Döring system," J. Stat. Phys. **132** (3), 519–533.

Soltzberg, Leonard J, Peter G. Bowers, and Christine Hofstetter (1997), "A computer model for soda bottle oscillations: "the bottelator"," J. Chem. Edu. **74** (6), 711 – 714.

Sowers, Kelly L, Brett Swartz, and Todd D. Krauss (2013), "Chemical mechanisms of semiconductor nanocrystal synthesis," Chem. Materials **25**, 1351–1362.

Sparks, R Stephen, and Herbert E. Huppert (1987), "The origin of granites," Nature **330**, 207–208.

Sugimoto, Tadao (1987), "Preparation of monodispersed colloidal particles," J. Coll. Interf. Sc. **28** (1), 65–108, Matijevic

Festschrift.

Sugimoto, Tadao (1992), "The theory of the nucleation of monodisperse particles in open systems and its application to AgBr systems," J. Coll. Interf. Sc. **150** (1), 208 – 225.

Sugimoto, Tadao, Fumiyuki Shiba, Tomohisa Sekiguchi, and Hiroyuki Itoh (2000), "Spontaneous nucleation of monodisperse silver halide particles from homogeneous gelatin solution I: silver chloride," Coll. Surf. A: Physchem. Eng. Aspects **164** (2 – 3), 183 – 203.

Toramaru, Atsushi, and Kazuki Maeda (2013), "Mass and style of eruptions in experimental geysers," J. Volcanology Geothermal Res. **257**, 227–239.

Vollmer, Jürgen (2008), "Phase separation under ultra-slow cooling: Onset of nucleation," J. Chem. Phys. **129** (16), 164502.

Vollmer, Jürgen, Günter K. Auernhammern, and Doris Vollmer (2007), "Minimal model for phase separation under slow cooling," Phys. Rev. Lett. **98**, 115701.

Vollmer, Jürgen, Doris Vollmer, and Reinhardt Strey (1997), "Oscillating phase separation in microemulsions II: Description by a bending free energy," J. Chem. Phys. **107** (9), 3627–3633.

Voorhees, Peter W (1985), "The theory of Ostwald ripening," J. Stat. Phys. **38** (1 – 2), 231 – 252.

Wagner, Carl (1961), "Theorie der Alterung von Niederschägen durch Umlösen (Ostwald-Reifung)," Z. Elektrochemie **65** (7 – 8), 581 – 591.

Zhang, Youxue, and Zhengjiu Xu (2008), ""Fizzics" of bubble growth in beer and champagne," Elements **4** (4), 47 – 49.

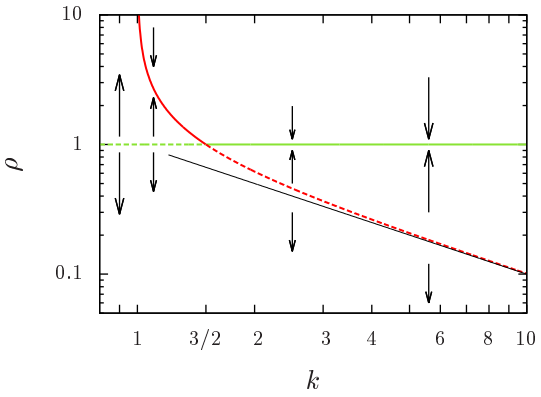
10
1
0.1
ρ
1
3/2
2
3
4
6
8
10
k

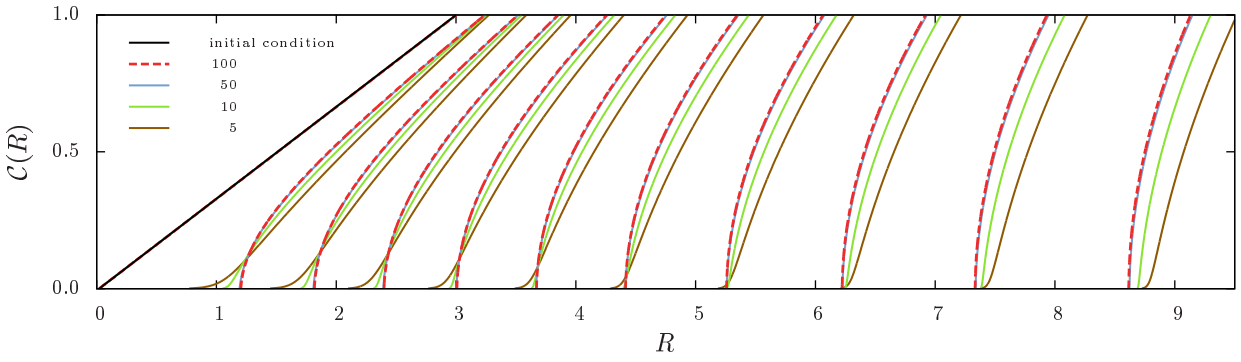
initial condition
100
50
10
5
1.0
0.5
0.0
$\mathcal{C}(R)$
0
1
2
3
4
5
6
7
8
9
R

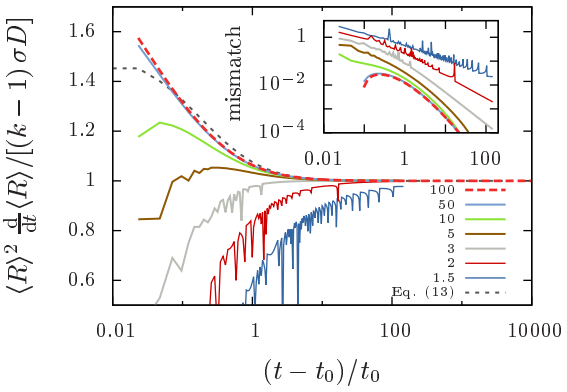
$\langle R\rangle^2 \frac{\mathrm{d}}{\mathrm{d}t}\langle R\rangle/[(k-1)\sigma D]$
1.6
1.4
1.2
1
0.8
0.6
0.01
1
100
10000
$(t-t_0)/t_0$
mismatch
1
10^{-2}
10^{-4}
0.01
1
100
100
50
10
5
3
2
1.5
Eq. (13)

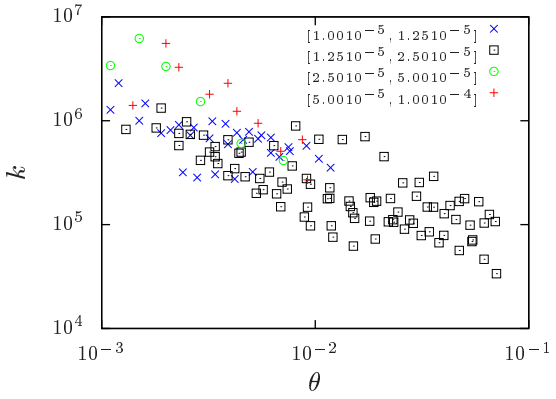
10^7
10^6
10^5
10^4
k
10^{-3}
10^{-2}
10^{-1}
θ
$[1.0010^{-5}, 1.2510^{-5}]$
$[1.2510^{-5}, 2.5010^{-5}]$
$[2.5010^{-5}, 5.0010^{-5}]$
$[5.0010^{-5}, 1.0010^{-4}]$

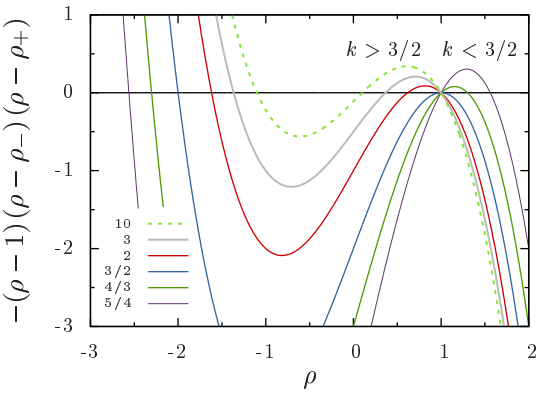
$-(\rho-1)(\rho-\rho_-)(\rho-\rho_+)$
ρ
$k > 3/2$
$k < 3/2$
10
3
2
3/2
4/3
5/4
1
0
-1
-2
-3
-3
-2
-1
0
1
2

(d)

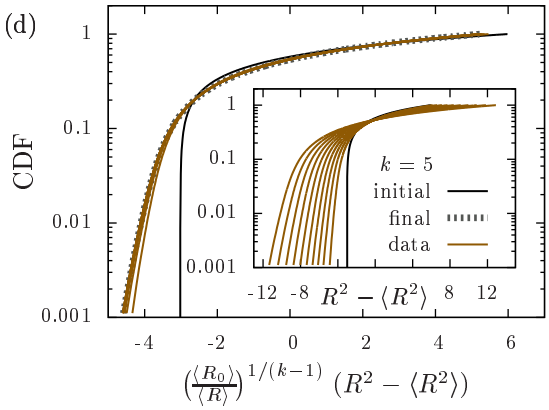
CDF
1
0.1
0.01
0.001
-4
-2
0
2
4
6
$\left(\frac{\langle R_0\rangle}{\langle R\rangle}\right)^{1/(k-1)}\ (R^2-\langle R^2\rangle)$
1
0.1
0.01
0.001
-12
-8
8
12
$R^2-\langle R^2\rangle$
$k=5$
initial
final
data

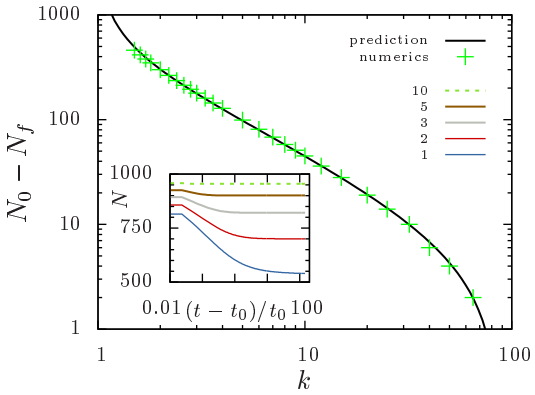
1000
100
10
1
$N_0 - N_f$
1
10
100
k
prediction
numerics
10
5
3
2
1
1000
750
500
N
0.01
$(t - t_0)/t_0$
100

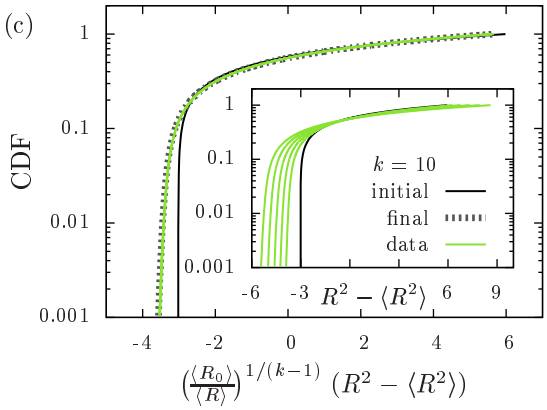
(c)
CDF
1
0.1
0.01
0.001
-4
-2
0
2
4
6
$\left(\frac{\langle R_0\rangle}{\langle R\rangle}\right)^{1/(k-1)}(R^2-\langle R^2\rangle)$
$k = 10$
initial
final
data
-6
-3
$R^2-\langle R^2\rangle$
6
9

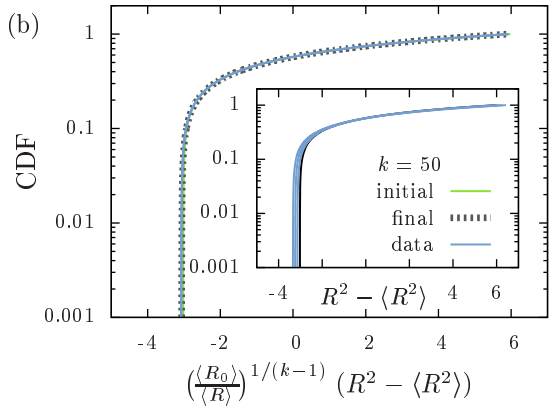
(b)
CDF
1
0.1
0.01
0.001
-4
-2
0
2
4
6
$\left(\frac{\langle R_0\rangle}{\langle R\rangle}\right)^{1/(k-1)}(R^2-\langle R^2\rangle)$
$k = 50$
initial
final
data
$R^2-\langle R^2\rangle$

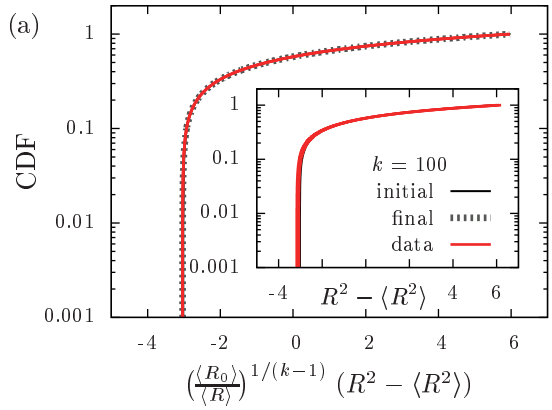
(a)
CDF
1
0.1
0.01
0.001
-4
-2
0
2
4
6
$\left(\frac{\langle R_0\rangle}{\langle R\rangle}\right)^{1/(k-1)}(R^2-\langle R^2\rangle)$
$k = 100$
initial
final
data
$R^2-\langle R^2\rangle$